

FULL ARTICLE

Monte Carlo simulation of *in vivo* Raman spectral measurements of human skin with a multi-layered tissue optical model

Shuang Wang^{1,2}, Jianhua Zhao^{2,3}, Harvey Lu^{2,3}, Qingli He⁴, Jintao Bai¹, and Haishan Zeng^{*,2,3}

¹ Institute of Photonics and Photon-Technology, The cultivation base of the state key laboratory of optoelectronic technology and functional materials co-constructed by Ministry of Education and Shaanxi Province, Northwest University, Xi'an, Shaanxi, China

² Imaging Unit – Integrative Oncology Department, British Columbia Cancer Agency Research Centre, Vancouver, BC, Canada

³ Photomedicine Institute – Department of Dermatology and Skin Science, University of British Columbia & Vancouver Coastal Health Research Institute, Vancouver, BC, Canada

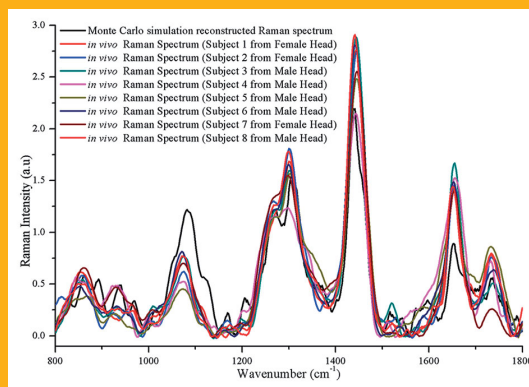
⁴ Department of Physics, Northwest University, Xi'an, Shaanxi, China

Received 18 March 2013, revised 10 September 2013, accepted 12 November 2013

Published online 6 December 2013

Key words: Monte Carlo simulation, Tissue Raman spectroscopy, Skin optical model, Intrinsic Raman of skin

Raman photon generation inside human skin and escaping to skin surface were modeled in an eight-layered skin optical model. Intrinsic Raman spectra of different skin layers were determined by microscopy measurements of excised skin tissue sections. Monte Carlo simulation was used to study the excitation light distribution and intrinsic Raman signal distortion caused by tissue reabsorption and scattering during *in vivo* measurements. The simulation results demonstrated how different skin layers contributed to the observed *in vivo* Raman spectrum. Using the strongest Raman peak at 1445 cm^{-1} as an example, the simulation suggested that the integrated contributions of the stratum corneum layer is 1.3%, the epidermis layer 28%, the dermis layer 70%, and the subcutaneous fat layer 1.1%. Reasonably good matching between the calculated spectrum and the measured *in vivo* Raman spectra was achieved, thus demonstrated great utility of our modeling method and approaches for help understanding the clinical measurements.



Comparison of the reconstructed Raman spectrum by Monte Carlo simulation with the measured *in vivo* Raman Spectra from different volunteers. The close matching of the spectra verified the utility of the modelling.

FULL ARTICLE

Monte Carlo simulation of *in vivo* Raman spectral measurements of human skin with a multi-layered tissue optical model

Shuang Wang^{1,2}, Jianhua Zhao^{2,3}, Harvey Lui^{2,3}, Qingli He⁴, Jintao Bai¹, and Haishan Zeng^{*,2,3}

¹ Institute of Photonics and Photon-Technology, The cultivation base of the state key laboratory of optoelectronic technology and functional materials co-constructed by Ministry of Education and Shaanxi Province, Northwest University, Xi'an, Shaanxi, China

² Imaging Unit – Integrative Oncology Department, British Columbia Cancer Agency Research Centre, Vancouver, BC, Canada

³ Photomedicine Institute – Department of Dermatology and Skin Science, University of British Columbia & Vancouver Coastal Health Research Institute, Vancouver, BC, Canada

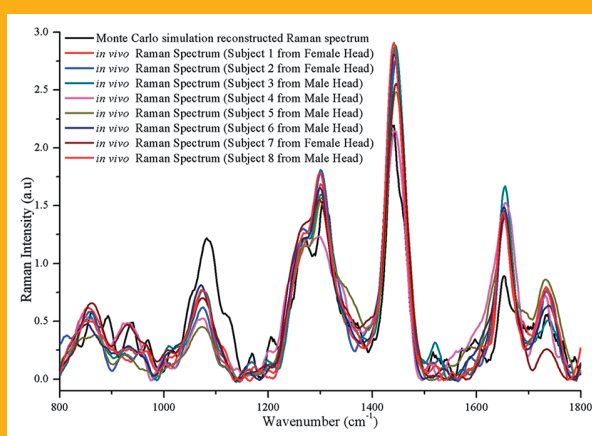
⁴ Department of Physics, Northwest University, Xi'an, Shaanxi, China

Received 18 March 2013, revised 10 September 2013, accepted 12 November 2013

Published online 6 December 2013

Key words: Monte Carlo simulation, Tissue Raman spectroscopy, Skin optical model, Intrinsic Raman of skin

Raman photon generation inside human skin and escaping to skin surface were modeled in an eight-layered skin optical model. Intrinsic Raman spectra of different skin layers were determined by microscopy measurements of excised skin tissue sections. Monte Carlo simulation was used to study the excitation light distribution and intrinsic Raman signal distortion caused by tissue reabsorption and scattering during *in vivo* measurements. The simulation results demonstrated how different skin layers contributed to the observed *in vivo* Raman spectrum. Using the strongest Raman peak at 1445 cm^{-1} as an example, the simulation suggested that the integrated contributions of the stratum corneum layer is 1.3%, the epidermis layer 28%, the dermis layer 70%, and the subcutaneous fat layer 1.1%. Reasonably good matching between the calculated spectrum and the measured *in vivo* Raman spectra was achieved, thus demonstrated great utility of our modeling method and approaches for help understanding the clinical measurements.



Comparison of the reconstructed Raman spectrum by Monte Carlo simulation with the measured *in vivo* Raman Spectra from different volunteers. The close matching of the spectra verified the utility of the modelling.

* Corresponding author: e-mail: hzeng@bccrc.ca, Phone: +1 604 675 8083, Fax: +1 604 675 8099

1. Introduction

In recent years there has been a remarkable increase in the application of optical spectroscopic methods (e.g. fluorescence, diffuse reflectance, elastic scattering and Raman scattering) for cancer and precancer detection and evaluation [1–3]. Different from the other methods, Raman spectroscopy measures inelastic light scattering, and is a vibrational spectroscopic technique that can provide very specific spectral fingerprints based on the molecular compositions of biological tissues [4, 5]. Since the fingerprinting-type narrow spectral features of Raman spectroscopy are very specific for different types of tissue biochemical changes, it has been used to successfully differentiate a variety of tissue pathologies of different organs [4, 5], of which skin provides an ideal measurement site for this optical technique, due to its easy accessibility. Furthermore, recent technical advances in Raman spectrometer hardware and probe design have paved the way for exploiting the Raman effects in clinical applications [6, 7]. For *in vivo* measurements the detected Raman signal is altered by the absorption and scattering of the heterogeneous structure and biochemical constituents of skin tissue, when the optical probe is placed on the skin surface. Therefore, it is essential to have an accurate model for illustrating the properties of photon propagation, Raman excitation, and Raman photon escape process in order to achieve a complete understanding of the *in vivo* spectral measurements.

Monte Carlo simulations are known to be effective in studying the skin autofluorescence measurements, by using microscopic scale fluorophore distributions and measured local intrinsic spectra in combination with skin optical parameters [8–10]. Recently, Monte Carlo and other mathematical models of Raman scattering have been applied to multi-layered biological tissues [11–12]. Starting from the photon migration theory, Feld et al. [13] derived an expression for the intrinsic Raman spectrum, utilized Monte Carlo simulations to demonstrate its validity, and elucidated the relationship between observed Raman and diffuse reflectance for semi-infinite samples and samples of finite dimension. Everall et al. [14] has applied Monte Carlo simulations to study time-resolved Raman and Tyndall photon migration in opaque samples under isotropic and forward scattering conditions. Wilson et al. [15] built a layered Monte Carlo model for Raman scattering to quantitatively understand the effect of overlying tissue layers on the detected bone Raman signal. Matousek et al. [16] proposed the first elementary model to illustrate Raman intensity variations for spatially offset Raman spectroscopy by performing Monte Carlo simulation. Keller et al. [17] designed a Monte Carlo model to investigate the effects of tissue and probe geometry on spatially offset Raman spectroscopy

(SORS) for breast tumor margin evaluation and found that SORS could detect submillimeter-thick tumors under a 1 mm normal tissue layer and 1 mm thick tumors under a 2 mm normal tissue layer. Reble et al. [18] designed a Monte Carlo model and calculated the depth dependent sensitivity or sampling volume of different single fibre and multi-fibre Raman probes based on a two-layer skin model. They found that the shape of the sampling volume was mainly determined by the scattering coefficient, while the wavelength-dependent absorption and scattering had a small effect on the sample volume [18]. Mo et al. [19] designed a Monte Carlo model for endoscopic fibre-optic probe and found that a ball lens could facilitate the depth-selected Raman measurement and fluorescence measurement. However, none of the above mentioned modeling considered inhomogeneous Raman scatter distributions in tissue. Different tissue layers have different Raman active molecules with different intrinsic spectra, thus will contribute differently to the measured *in vivo* spectra. We will deal with this issue in our modeling to achieve better understanding of the *in vivo* Raman measurements.

In this study, we modeled the *in vivo* Raman measurement of normal human skin in the near infrared (NIR) wavelength range. An eight-layer skin optical model was built with transport parameters adapted from a number of publications. Calculation of 785 nm excitation light distribution inside the model was performed directly with Monte Carlo code from Wang and Jacques [20, 21]. The code was modified to simulate the Raman escape process. Raman spectra of *ex vivo* normal skin tissue sections were measured to quantify the different intrinsic micro-spectral properties of different skin layers [22]. The reconstructed skin Raman spectrum was compared with clinically measured *in vivo* skin spectra to verify the utility of the modelling.

2. Materials and methods

2.1 *In vivo* measurement of human skin Raman spectrum

The setup used for *in vivo* Raman measurements has been described in detail elsewhere [6, 7, 23]. The Raman system consists of a 785 nm diode laser (BRW-785-1.0-100-0.22-SMA, B&W, Tek Inc.), a transmissive imaging spectrograph (HoloSpec-f/2.2-NIR, Kaiser), a NIR-optimized, back illuminated, deep-depletion, CCD detector (LN/CCD-1024EHRB, Princeton Instruments), and a specially designed Raman probe. The laser is coupled to our Raman probe via a 200 μm core-diameter fibre. The spot size of the laser on skin

is around 3.5 mm in diameter, with a laser power less than 150 mW, below the ANSI laser safety standard. Signal from about 1.3 mm in diameter in the center of the laser spot is measured [24]. Skin-scattered Raman photons are collected from the probe by a fibre bundle (N.A., 0.22) and fed into the spectrograph, whereupon the photons are dispersed on to the CCD array detector by a volume-phase technology holographic grating. A PC controls the CCD detector and spectral data acquisition, processing, and display. The CCD, with enhanced quantum efficiency and reduced etaloning in the NIR (quantum efficiency, $\leq 75\%$ at 900 nm), was liquid-nitrogen cooled to remove thermal noises. The CCD consisted of 1024×256 pixels ($27 \mu\text{m} \times 27 \mu\text{m}$) and allowed vertical binning for improved detection sensitivity. The whole system was packed onto a movable cart for outpatient clinical data acquisition. *In vivo* clinical measurements were carried out in the Skin Care Centre of the Vancouver General Hospital, Vancouver, Canada. Informed consent has been obtained from each subject measured. The study was approved by the University of British Columbia Clinical Research Ethics Board (Certificate # H96-70499).

2.2 *Ex vivo* measurements of Raman spectra from excised human skin tissue sections

A home-made modular microspectroscopy system is used to measure *ex vivo* skin tissue sections [22]. The system setup is schematically shown in Figure 1. Its major components include a fibre-coupled diode laser (BRW-785-1.0-100-0.22-SMA, B&W, Tek Inc.), an inverted microscope (Diaphot, Nikon), a trans-

missive imaging spectrograph (HoloSpec-f/2.2-NIR, Kaiser), and a CCD camera (Spec-10:100BR/LN, Princeton Instruments). A fibre bundle was designed to deliver the signals to the spectrograph. The fibre bundle was composed of thirty seven (37) $40 \mu\text{m}$ core-diameter optical fibres, packed into a circular area of $385 \mu\text{m}$ in diameter in the microscope side, and aligned into two closely-packed columns in the spectrograph side to enhance the detection of the inherently low Raman signals. In order to battle the background fluorescence from the system, conventional normal illumination was replaced by oblique illumination at 45° and the microscope slides were coated with gold. These modifications substantially reduced the background from the slides and the system so that Raman spectra from skin tissue sections can be obtained.

For the measurements, the excitation spot on the tissue was around 2 mm in diameter, and the Raman signal collection spot size was about $15.4 \mu\text{m}$ diameter for a $10\times$ objective and the $385 \mu\text{m}$ collection fibre bundle we choose. Spectral signals could be collected over the range of $800\text{--}1800 \text{ cm}^{-1}$. The fluorescence signal is overlapped with the narrow and weak Raman peaks, which can be removed automatically by a specially-designed polynomial fitting method – the Vancouver Raman Algorithm [24]. A fresh skin sample obtained from excised tissue during facial surgery was frozen and cut into sections of about $20 \mu\text{m}$ thick (unstained and unfixed), and then placed on gold coated microscope slides for examination. NIR fluorescence images of the skin sections were also recorded using a computer-controlled NIR-sensitive CCD camera (AltaU1, Apogee Instruments) connected to the microscope to help better identify different skin layers.

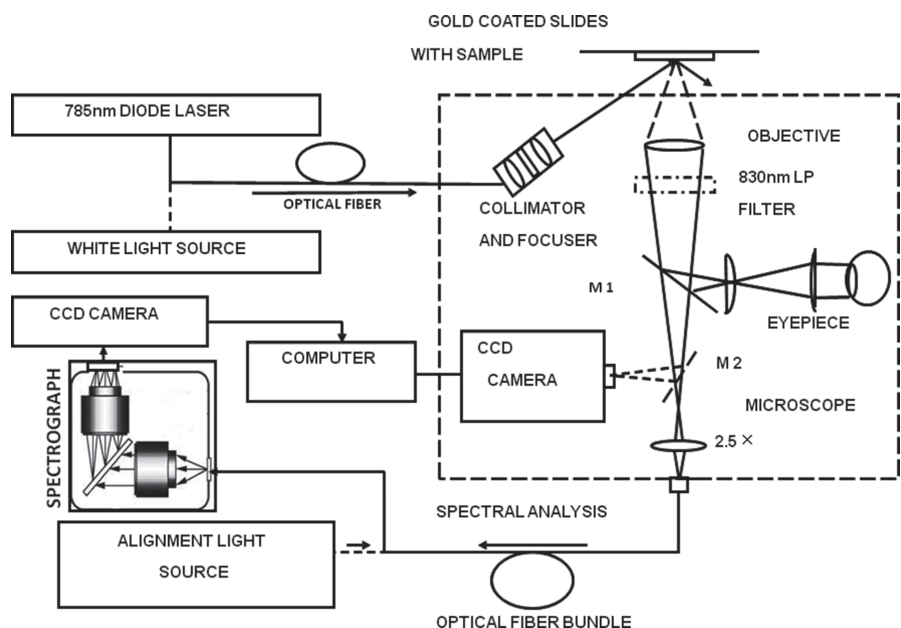


Figure 1 Setup of the custom-made microspectroscopy system. Reproduced from Ref. [22] with permission.

2.3 Optical model of normal human skin

The skin is a layered structure interspersed with various appendages such as hair follicles, sweat glands, and sebaceous glands, which we will ignore for simplicity but without loss of generality. We have published a systematic study on the modeling of light propagation and light-tissue interaction in normal human skin [8–10]. In this work, we developed an eight-layer skin optical model in the NIR wavelength range with transport parameters compiled from Salomatina et al. [25] and Meglinski et al. [26]. Table 1 outlines this eight layer model, including thickness (d), refractive index (n), and the optical transport parameters (absorption coefficient, μ_a , scattering coefficient, μ_s , scattering anisotropy, g) at 840 nm for each skin layer. For this study, 785 nm is the wavelength of the laser light used for Raman excitation. Skin Raman spectra from 800 cm^{-1} to 1800 cm^{-1} , which is corresponding to the wavelength range from 838 nm to 914 nm, is reconstructed by Monte Carlo method to investigate how the intrinsic Raman signals originated from different skin layers contribute to the *in vivo* signal and how are they distorted by the tissue reabsorption and scattering during *in vivo* measurements. The total thickness of the skin model is 5 mm [27], while the thickness of each layer is based on the microscopic measures and anatomical studies from our group and published literatures.

The refractive index of the ambient medium above the 8-layer tissue is 1.0, which is assumed to be air, and the ambient medium below the 8-layer tissue is 1.37 [27], which is assumed to be muscle. In the skin model, we assumed that anisotropy factor g was 0.8 for all the bloodless skin layers in the entire investigated wavenumber range [10]. The refractive index was 1.4 in both epidermis and dermis layers based on a water content of 70–80% [8], 1.45 for stratum corneum layer [8], and 1.46 for subcutaneous layer [8, 10]. The optical properties of normal

skin have been investigated by several groups [26, 28, 29]. Although the data for optical transport parameters of epidermis and stratum corneum in NIR wavelength are rare [30, 31], it is well established that skin absorption in NIR spectral region is dominated by oxy-/deoxy-haemoglobin and water [26]. Therefore, as a blood-free layer, the absorption coefficient of stratum corneum could be calculated as [26]:

$$\mu_a^{\text{stratum}}(\lambda) = ((0.1 - 0.3 \times 10^{-4}\lambda) + 0.125\mu_a^{(0)}(\lambda)) \times (1 - C_{\text{H}_2\text{O}}) + C_{\text{H}_2\text{O}}\mu_a^{\text{H}_2\text{O}}(\lambda) \quad (1)$$

where $\mu_a^{\text{stratum}}(\lambda)$ is the absorption coefficient of stratum corneum; λ is the wavelength of light; $C_{\text{H}_2\text{O}}$ is the volume fraction of the water in stratum corneum [32, 33], which is 0.05; $\mu_a^{\text{H}_2\text{O}}(\lambda)$ is the absorption coefficient of water as a function wavelength; $\mu_a^{(0)}(\lambda)$ is the absorption coefficient caused by the intrinsic absorption of the hemoglobin-water free tissue, defined as [26, 34]

$$\mu_a^{(0)} = 7.84 \times 10^7 \times \lambda^{-3.255} \quad (2)$$

The calculated results agree well with experimental results for Caucasian skin [35], showing that absorption of the visible/NIR radiation in stratum corneum decreases uniformly within wavelength range from 450 nm to 900 nm. Therefore, we calculated the absorption coefficient of stratum corneum at different wavelength by this way. However, there is no published data for the scattering coefficient of stratum corneum. In this study, it was assumed that the scattering coefficient of stratum corneum was the same as that of the epidermis. This assumption should not cause much error because the stratum corneum layer is very thin (10 μm).

The refractive index of blood was assumed to be 1.33, which is equivalent to that of water. For all the layers of the epidermis, blood-free dermis, and subcu-

Table 1 The transport parameters (μ_a , μ_s , g , n) at 840 nm of the eight-layer skin optical model.

Layer	D (μm)	n	μ_s (cm^{-1})	μ_a (cm^{-1})	g
Air	–	1.0	–	–	–
Stratum Corneum	10	1.45	176.125	0.7405	0.8
Epidermis	80	1.4	176.125	1.3	0.8
Papillary Dermis	100	1.4	106.25	1.05	0.8
Upper Blood Plexus	80	1.39	145.625	1.427	0.818
Reticular Dermis	1500	1.4	106.25	1.05	0.8
Deep Blood Plexus	70	1.34	460.625	4.443	0.962
Lower Dermis	160	1.4	106.25	1.05	0.8
Subcutaneous Fat	3000	1.46	97.125	0.975	0.8
Muscle	–	1.37	–	–	–

taneous fat, the transport parameters from 370 nm to 1570 nm were provided by Salomatina et al. [25]. The upper blood plexus consists of capillaries scattered inside the dermal tissue. Therefore, it was modeled as a uniform layer of 10% blood and 90% dermal tissue. The optical parameters (μ_a, μ_s, g, n) of the upper blood plexus were calculated by adding the fractional contributions of the two components [36], which can be expressed by the following matrix formula [8–10]:

$$\begin{bmatrix} \mu_a \\ \mu_s \\ g \\ n \end{bmatrix} = \begin{bmatrix} \mu_a^1 & \mu_a^2 \\ \mu_s^1 & \mu_s^2 \\ g^1 & g^2 \\ n^1 & n^2 \end{bmatrix} \cdot \begin{bmatrix} f_1 \\ f_2 \end{bmatrix} \quad (3)$$

where f_1 and f_2 are the percentages of individual component, respectively. For example, the upper blood plexus took up 10% blood ($f_1 = 0.1$) and 90% dermal tissue ($f_2 = 0.9$) in the optical tissue model [8–10, 36]. So the refractive index of the upper blood plexus was estimated to be $n = 1.4 \cdot 0.09 + 1.33 \cdot 0.10 = 1.39$. The lower blood plexus was modeled as consisting of 90% blood and 10% dermis tissue. To model the Raman escape process, tissue optical parameters at other wavelengths were derived in a similar fashion.

In this work, in order to investigate the skin Raman properties, we compiled the data of each skin layer at 18 wavelengths from 838 to 914 nm, corresponding to 800 cm^{-1} to 1800 cm^{-1} in wavenumber under 785 nm excitation using the data compiled from Salomatina et al. [25]. In order to give a detailed description of the simulated Raman spectrum, an interpolation was carried out to get the same number of data points as the Raman spectrum from *ex vivo* measurements [22].

2.4 Monte Carlo simulation

The Monte Carlo code from Wang and Jacques [20, 21] were used to calculate the responses of the eight-layered skin model to a 785 nm light beam incident on the surface. Excitation light distribution inside the skin was calculated directly by the code. All simulations were carried out in the unit of wavelength (nm), whereas simulated results were presented in the unit of wavenumber (cm^{-1}) for consistency with the experimental results. Furthermore, the Monte Carlo code is modified to simulate the launch of photons from a buried isotropic source for modeling the Raman scattering within the tissue. The Raman photon escape process is assumed to be the same as fluorescence photon escape from inside the tissue. Therefore, the same modeling procedures developed in our previous work on fluorescence simulation [8–10] were used for the Raman simulation, which consists of the following steps:

(1) Calculate the excitation light distribution inside the model skin, $\Phi(\lambda_{\text{ex}}, r, z, \theta)$. This is performed directly with the Monte Carlo code from Wang and Jacques [20, 21]. It is in units of W/cm^2 , λ_{ex} is the excitation wavelength, while r, z, θ represent local positions in the cylindrical coordinates.

(2) Calculate escape functions for different wavelengths and at different depths, $E(\lambda_{\text{em}}, r, z)$. The Monte Carlo code was modified to simulate the light propagation process for an isotropic Raman point source buried at depth z inside the tissue. After integrating with respect to r and θ in the cylindrical coordinate, the escape function can be simplified as a function of emission wavelength and depth, $E(\lambda_{\text{em}}, z)$, where λ_{em} is the emission wavelength. We studied 18 different wavelengths from 838 nm to 914 nm, corresponding to the wavenumber from 800 cm^{-1} to 1800 cm^{-1} under 785 nm excitation. For each Raman emission wavelength, 106 different depths were simulated so as to cover the whole skin model thickness.

(3) Calculate Raman detection efficiency, $\eta(\lambda_{\text{em}}, z)$, as a function of wavelength for different skin layers. The Raman detection efficiency was defined as the likelihood of obtaining a Raman signal from a specific skin layer. It does not include the intrinsic spectral line shape. Instead, it illustrates how the intrinsic Raman spectra are distorted by the tissue reabsorption and scattering during the escape process. It is an integral of the product of the excitation light distribution inside the tissue and the Raman escape function.

$$\eta_{\text{layer: } z_1 \rightarrow z_2}(\lambda) = \int_{z_1}^{z_2} \Phi(z) E(\lambda, z) dz \quad (4)$$

where $z_2 - z_1 = \Delta z$ is the thickness of different skin layers.

(4) Calculate the simulated Raman spectra, $R(\lambda_{\text{ex}}, \lambda_{\text{em}}, r)$. The reconstructed *in vivo* Raman spectrum of skin tissue is a linear combination of the product of intrinsic spectrum and the Raman detection efficiency of all the excited molecules. The intrinsic Raman spectrum of any skin layer, $\beta(\lambda_{\text{ex}}, \lambda_{\text{em}}, z)$, could be measured from excised human skin tissue sections by a modular microspectroscopy system shown in Figure 1. The simulated Raman spectrum is computed by the convolution of the excitation light distribution, the intrinsic Raman spectrum, and the Raman escape function:

$$\begin{aligned} R(\lambda_{\text{ex}}, \lambda_{\text{em}}, r) &= \int_0^D \int_0^{2\pi} \int_0^\infty \Phi(\lambda_{\text{ex}}, r', z', \theta) \beta(\lambda_{\text{ex}}, \lambda_{\text{em}}, z') \\ &\quad \times E(\lambda_{\text{em}}, \sqrt{r^2 + r'^2 - 2rr' \cos \theta'}, z') r' dr' d\theta' dz' \end{aligned} \quad (5)$$

where D is the total thickness of the model skin.

3. Results and discussions

Monte Carlo simulation were performed to record the excitation photon transmittance and fluence deposit inside the model skin for 785 nm excitation light and for escape functions at 106 different Raman source depths and 15 different emission wavelengths at an interval of 5 nm from 840 nm to 910 nm. Also, in order to cover main Raman emission peaks in the range of 800–1800 cm^{-1} under 785 nm excitation, three more simulation points, which are 838, 858 and 914 nm, were added in the simulation process corresponding to 800, 1080 and 1800 cm^{-1} . Thus, a totally 1908 simulations (18×106) had to be performed to reconstructed *in vivo* Raman spectrum, requiring a large amount of calculations. In each simulation, 1,000,000 photons were launched.

The edge effects for the Raman detection was neglected in that a relative wider illumination beam and a smaller detection spot were used in our clinical measurements [6, 7, 23]. Therefore, the excitation light distribution could be simplified as a function of z only, i.e. $\Phi(z)$, during the simulation. The z axis is perpendicular to the skin surface and represents the depth within the skin. Figure 2 shows the excitation light (785 nm) distribution $\Phi(z)$ inside the skin tissue. Due to back-scattering effect, the fluence in the stratum corneum is about 3.7 times of the incident fluence showing the photon pile-up near the air-tissue interface. Since the scattering is dominant over absorption in the light-tissue interaction in this skin model, it can be seen that some photons could still penetrate into the deep subcutaneous fat; however its fluence at the bottom of subcutaneous fat is only about 2% of the value at the stratum corneum.

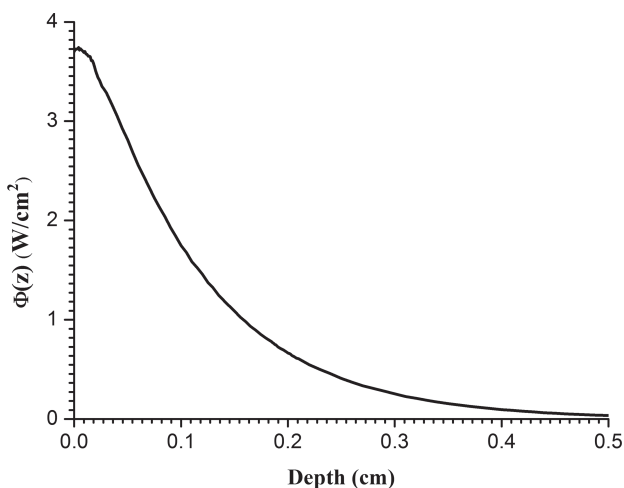


Figure 2 Monte Carlo simulation results of the excitation laser light (785 nm) distribution in skin tissue (infinite wide beam, normal incidence). The incident power density is 1 W/cm^2 .

Once a Raman scattering effect is occurred and a Raman photon is emitted, it has to escape the skin surface to be observed. It can be regarded as an isotropic source buried in the skin tissue. The Monte Carlo program was modified to accommodate the light propagation at 106 different depths to calculate the escape function, $E(\lambda_{\text{em}}, z)$ in the 838 nm to 914 nm wavelength range. Five depth levels were simulated for the stratum corneum layer at 2 μm intervals. Eight depth levels were simulated for the epidermis layer at 10 μm intervals. Ten depth levels were simulated for the papillary dermis at 10 μm intervals. Eight depth levels were simulated for the upper blood plexus layer at 10 μm intervals. Thirty depth levels were simulated for the reticular dermis layer at 50 μm intervals. Seven depth levels were simulated for the deep blood plexus layer at 10 μm intervals. Eight depth levels were simulated for the lower dermis layer at 20 μm intervals. Thirty depth levels were simulated for the subcutaneous fat layer at 100 μm intervals. The calculated Raman escape efficiency, $E(\lambda_{\text{em}}, z)$, was expressed as a function of the emission wavelength λ_{em} at specific depth z inside the tissue, as shown in Figure 3. Figure 3a shows that $E(\lambda_{\text{em}}, z)$ has minimal dependence on λ_{em} near the tissue surface, indicating that reabsorption and scattering of the Raman photons near the skin surface have minimal effect on the Raman escape function. Figure 3a also shows that in general $E(\lambda_{\text{em}}, z)$ decreases as tissue depth increases. However, it is very interesting to notice that the escape efficiency is slightly increased at the depth of 0.28 cm, which is more clearly exhibited in Figure 3b. This maximum located in the subcutaneous fat layer can be explained by the unique refractive index changes before and after this tissue layer. In general, the escape function should have a decreasing trend with increasing depth inside the tissue because the deeper the Raman source, the more difficult for the photons to escape out of the tissue surface. However, the sudden refractive index changes at the boundaries of different tissue layers can have effects against this trend. Particularly for the subcutaneous layer, its refractive index is higher than both its upper layer and lower layer. In this situation, some of Raman photons generated inside this layer will encounter total internal reflection that completely bounces these photons back. The total internal reflection effect at the upper boundary will make escape function decrease more near the surface, while the total internal reflection effect at the lower boundary will help the photon escape, therefore, count the general decreasing trend. The combination of all these factors makes it possible to produce a local maximum of the escape function somewhere within the layer. This explanation is further confirmed by the subtle, but consistent small shoulder shown on all the curves in Figure 3b around 0.035 cm depth, which is located

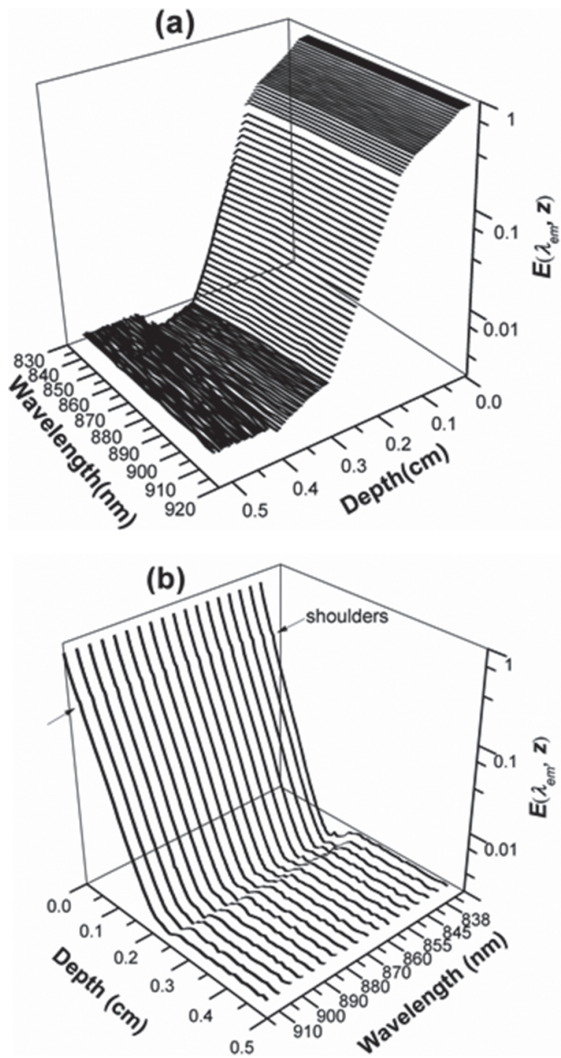


Figure 3 (a) Raman escape efficiency, $E(\lambda, z)$, plotted as a function of wavelength at specific depth inside the tissue; (b) Raman escape efficiency, $E(\lambda, z)$, plotted as a function of depth within the tissue at specific wavelength. The results were calculated by Monte Carlo simulation.

inside the reticular dermis layer, the only other tissue layer with refractive index higher than both its upper and lower layers in the model skin.

In order to understand how the intrinsic Raman spectra are distorted by the tissue reabsorption and scattering, the Raman detection efficiency, $\eta(\lambda_{em}, z)$, which is the likelihood of obtaining a Raman signal from a specific layer at each simulation wavelength, is shown in Figure 4. Note that $\eta_{stratum\ corneum}$ and $\eta_{subcutaneous\ fat}$ are low, showing that stratum corneum and subcutaneous fat layers have less contribution to the observed *in vivo* Raman. This is understandable because although the stratum corneum layer is close to the skin surface, easy for its Raman photons getting escapes, it is much thinner than other layers. The majority of the Raman photons are generated

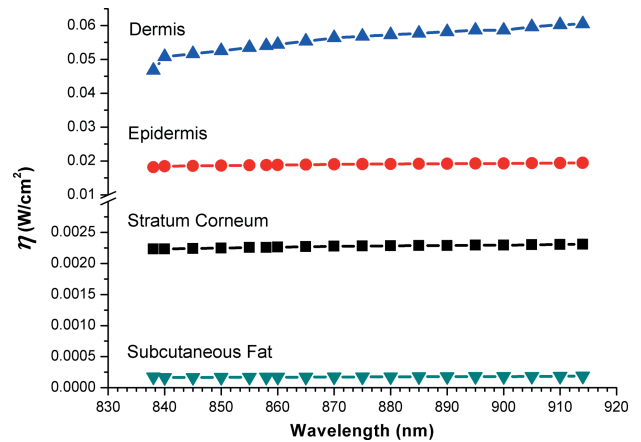


Figure 4 Monte Carlo simulated Raman detection efficiency, η , as a function of wavelength for the stratum corneum, epidermis, dermis and subcutaneous fat layer.

in the thicker layers such as the epidermis, dermis and subcutaneous fat layers. However, because the subcutaneous layer is deep in the tissue, the re-emitted Raman photons encounter more reabsorption and scattering by the above three layers when escaping towards the skin surface, making the detection efficiency lower. From Figure 4, we can also see that the detection efficiencies of the stratum corneum layer, the subcutaneous fat layer and the epidermis layer are almost independent of the emission wavelength. But the detection efficiency of the dermis layer is an increasing function of wavelength. This is in consistency with the decreasing trends of the absorption coefficients and the scattering coefficients with wavelength. The blood content that is located within this layer probably played a very important role. The curves for stratum corneum layer and the epidermis layer are flat because they are close to the surface and did not encounter much reabsorption and scattering. The subcutaneous curve is flat probably because of its deep location, where the reabsorption and scattering effects are saturated, thus much less dependent of wavelengths.

The intrinsic Raman coefficient, $\beta(\lambda_{ex}, \lambda_{em}, z)$ can be measured from *ex vivo* experimental studies. Figure 5 shows a pure Raman spectrum of unstained and fresh normal skin section excised from facial surgery [22]. Raman spectra were obtained from different skin layers on the section and NIR autofluorescence image was captured to identify its microscopic structure. Prominent spectral features in the range of 800–1800 cm^{-1} are the major vibration bands around 855, 935, 1080, 1265, 1311, 1445, 1650, and 1745 cm^{-1} , which stand for different molecular vibrational modes. Note that the Raman signals from the subcutaneous layer are about 4 to 5 times stronger than that of the epidermis and dermis. This means that they will have measurable contributions to the

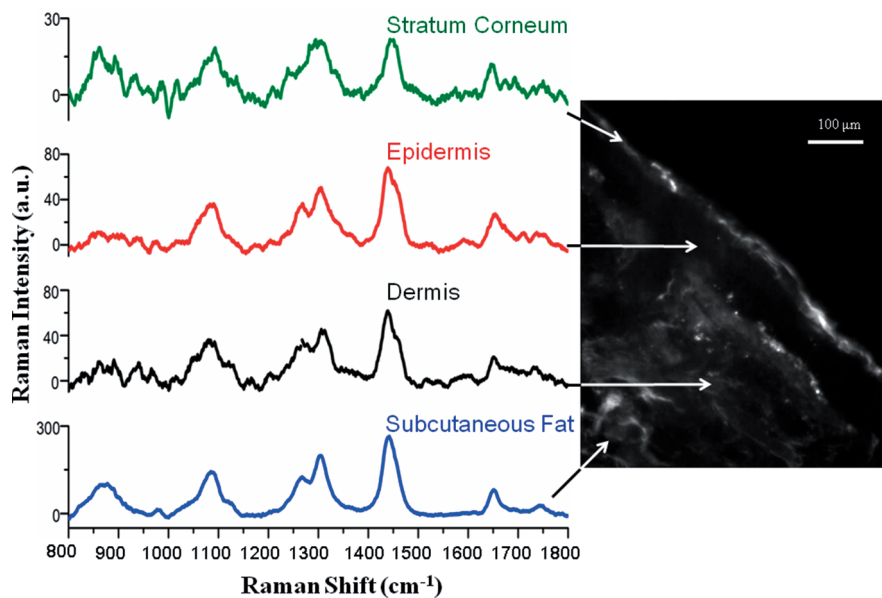


Figure 5 Intrinsic Raman spectrum measured from different layers of an unstained and fresh normal skin excised from facial surgery. NIR autofluorescence image of skin section was combined to show the spectra measurement location. Integration time is 30 s for each spectrum. Reproduced from Ref. [22] with permission.

in vivo Raman spectrum although the detection efficiency for this layer is the lowest (Figure 4). Although there are multiple sub-layers of the dermis in the model skin as outlined in Table 1, the same measured dermis spectrum shown in Figure 5 is used as the $\beta(\lambda_{\text{ex}}, \lambda_{\text{em}}, z)$ function for all sub-layers of the dermis in the model skin.

The *in vivo* Raman spectra from facial skin were measured from eight volunteers and are shown in Figure 6 for comparison. In order to minimize the system setup influence on the spectra deviations, the same spectral processing procedure as for the *ex vivo* microspectroscopy measurement was carried out for each *in vivo* measurement. The spectral response of the system was corrected using a standard tungsten-halogen lamp, and the laser intensity variation is also corrected. Raman frequencies were calibrated with cyclohexane, acetone, and barium sulphate to an accuracy of $\pm 2 \text{ cm}^{-1}$ [23]. The Vancouver Raman Algorithm [24] was utilized to remove the autofluorescence background and obtain the pure Raman spectra. Based on this procedure, the deviation of skin Raman spectra introduced by experimental setup could be reduced as much as possible. The *in vivo* facial skin Raman spectra are normalized to their respective area under the curve. It can be observed that the spectral shapes are different between *in vivo* and *ex vivo* results; however the major vibrational bands could be easily identified in both *in vivo* and *ex vivo* spectra.

In order to reconstruct *in vivo* Raman spectra using Eq. (5), an interpolation was carried out for the detection efficiencies shown in Figure 4 to get the same number of data points at the same wavenumbers as in the *ex vivo* spectra shown in Figure 5. Figure 7 shows the reconstructed Raman spectrum

compared with all the eight *in vivo* Raman measurements. The *in vivo* Raman spectra were normalized to their respective area under the curve. In general the reconstructed Raman spectrum matches reasonably well with the *in vivo* Raman spectra. In particular, the five major Raman peaks reconstructed by this Monte Carlo simulation around 855, 935, 1265, 1445, and 1745 cm^{-1} match very well with the *in vivo* spectra. There are also differences between the reconstructed and the *in vivo* Raman spectra. The main difference is seen around 900, 1080, and 1650 cm^{-1} bands. These differences may be due to

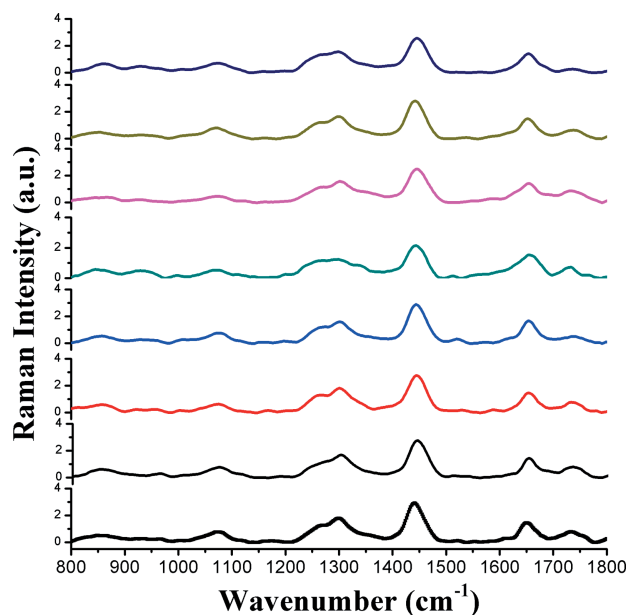
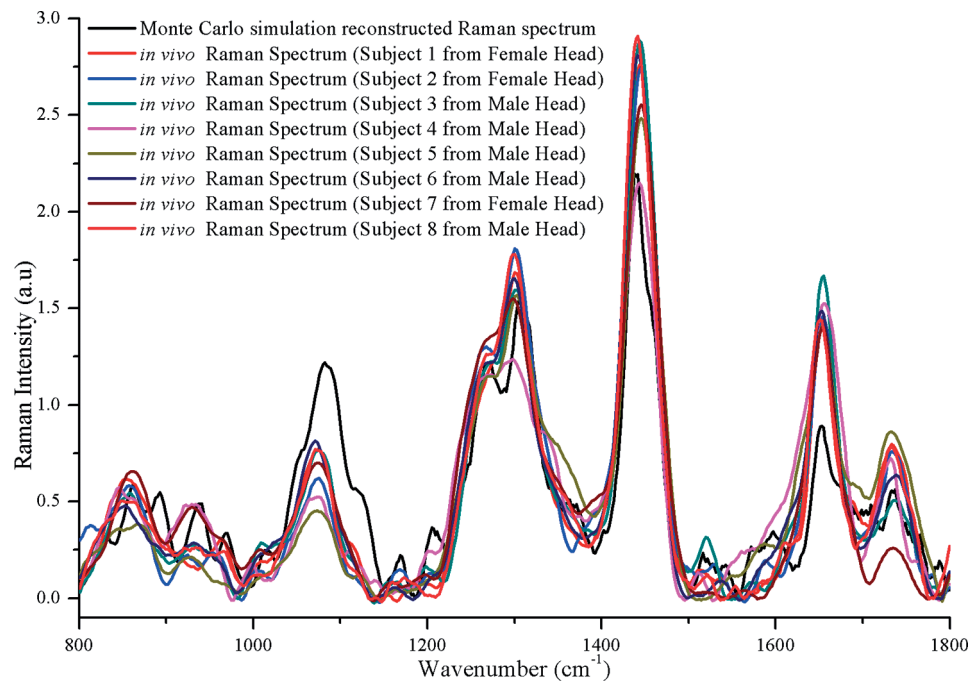


Figure 6 *In vivo* Raman spectra of facial skin tissue measured from eight volunteers.

Figure 7 Comparison of the reconstructed facial skin Raman spectrum by Monte Carlo simulation with eight *in vivo* Raman spectra of facial skin tissue.



the fact that the sample composition of the microscopic measurement is different from the *in vivo* tissues because they are not from the same subject. Another possible reason is the influence of instrument response calibration and background correction of both the macro-Raman and micro-Raman measurement. Further test is under investigation to evaluate the variations between the simulated and the measured spectrum. Based on these two reasons, we could see that the simulated Raman spectrum is in fairly good agreement with the *in vivo* Raman spectra. It suggests that the modelling method, the skin optical model, and the approach to determine the intrinsic Raman properties are justified.

It is interesting to see how much each skin layers have contributed to the measured *in vivo* Raman spectrum. Using the largest Raman peak (1445 cm^{-1}) as an example, the reconstructed data showed that the stratum corneum contributed 1.3%, the epidermis 28%, the dermis 70%, and the subcutaneous fat 1.1%.

4. Conclusion

In summary, the Raman properties of normal human skin were studied by Monte Carlo method. In the simulation, an eight-layer optical model was built to represent skin tissue. The photon propagation of the excitation light and re-emitted Raman light was modeled in this medium. Microspectroscopic Raman spectral measurements of excised skin tissue sections were used to generate the intrinsic Raman spectrum of individual skin layers. The reconstructed

Raman spectrum was obtained by convoluting the intrinsic spectra with the Monte Carlo simulation results of excitation light distribution and Raman photon escape efficiency. The simulation result suggests that the majority of the measured *in vivo* skin Raman signals comes from the dermis (70%) and the epidermis (28%). The stratum corneum, although very thin, still has non-negligible contributions (1.3%) due to its near surface location and thus, easy for the Raman photons to escape. The contribution of subcutaneous layer is also not negligible (1.1%) due to its much higher Raman scattering efficiencies than other tissue layers (4 to 5 times that of epidermis/dermis), although it is located deep inside the skin, making Raman photon escaping more difficult.

The reconstructed Raman spectrum reached reasonable good agreement with the measured *in vivo* skin spectra, demonstrating the utility of our modelling and experimental approaches. A primary shortcoming of the current model is that skin tissue had to be presented as a multilayered planar structure. In reality, skin tissue does not have planar boundaries with defined thickness of each layer and its measured microscopic and macroscopic Raman properties vary from person to person, and are also affected by many reasons, such as illumination geometry, fibre probe collection scheme, and influence from system correction, etc. Modelling a skin tissue with an 8 layer tissue structure is a reasonable step in investigating the excitation light distribution and intrinsic Raman signal distortion caused by tissue re-absorption and scattering during *in vivo* measurements. A major advantage of our work is that we

also incorporated the inhomogeneous Raman scatter distributions into the modelling and thus generated more realistic fractional contributions of each skin layer to the *in vivo* Raman spectrum.

Acknowledgements This work was supported by the Canadian Cancer Society, the Canadian Institutes of Health Research, the Canadian Dermatology Foundation, the Major Research Plan of the Natural Science Foundation of China (No. 91123030), the International Science & Technology Cooperation Program of China (No. 2011DFA12220), the Natural Science Fund of Shaanxi Province, China (No. 2010JK868), and the Natural Science Research Foundation of Northwest University, China (No. 12NW11). The authors wish to thank Dr. Anna Yaroslavsky of the Wellman Center for Photomedicine, Harvard Medical School for her kindly providing the NIR skin optical parameters. We also like to thank Wei Zhang for his technical assistance.

Author biographies Please see Supporting Information online.

References

- [1] J. C. Hebden, S. R. Arridge, and D. T. Delpy, *Phys. Med. Biol.* **42**, 825–840 (1997).
- [2] V. V. Tuchin, *Handbook of Optical Biomedical Diagnostics*. (SPIE Press, 2002), p. 443.
- [3] B. C. Wilson, V. V. Tuchin, and S. Tanev, *Advances in Biophotonics* (Ios Press Inc, 2005), p. 125.
- [4] J. Popp, C. Krafft, and T. Mayerhöfer, *Optik & Photonik* **6**, 24–28 (2011).
- [5] T. Dieing, O. Hollricher, and J. Toporski, *Confocal Raman Microscopy* (Springer, 2011), p. 23.
- [6] H. Lui, J. Zhao, D. I. McLean, and H. Zeng, *Cancer Res.* **72**, 2491–2500 (2012).
- [7] J. Zhao, H. Lui, D. I. McLean, and H. Zeng, *Skin Res. Tech.* **14**, 484–492 (2008).
- [8] H. Zeng, C. MacAulay, D. I. Mclean, and B. Palcic, *J. Photochem. Photobiol. B: Biol.* **38**, 234–240 (1997).
- [9] R. Chen, Z. Huang, H. Lui, I. Hamzavi, D. I. Mclean, S. Xie, and H. Zeng, *J. Photochem. Photobiol. B: Biol.* **86**, 219–226 (2007).
- [10] S. Wang, J. Zhao, H. Lui, Q. He, and H. Zeng, *J. Photochem. Photobiol. B: Biol.* **105**, 183–189 (2011).
- [11] I. Pavlova, C. R. Weber, R. A. Schwarz, M. D. Williams, A. M. Gillenwater, and R. Richards-Kortum, *J. Biomed Opt.* **14**, 014009 (2009).
- [12] I. Pavlova, C. R. Weber, R. A. Schwarz, M. D. Williams, A. El-Naggar, A. Gillenwater, and R. Richards-Kortum, *J. Biomed Opt.* **13**, 064012 (2008).
- [13] W. C. Shih, K. L. Bechtel, and M. S. Feld, *Opt. Express* **16**, 12726–12736 (2008).
- [14] N. Everall, T. Hahn, P. Matousek, A. W. Parker, and M. Towrie, *Appl. Spectrosc.* **58**, 591–597 (2004).
- [15] R. H. Wilson, K. A. Dooley, M. D. Morris, M. Mycek, in: *SPIE Proc. of Optics in Bone Biology and Diagnostics*, San Jose, US, February 2009. pp. 716604–716614.
- [16] P. Matousek, M. D. Morris, N. Everall, I. P. Clark, M. Towrie, E. Draper, A. Goodship, and A. W. Parker, *Appl. Spectrosc.* **59**, 1485–1492 (2005).
- [17] M. D. Keller, R. H. Wilson, M. Mycek, A. Mahadevan-Jansen, *Applied Spectroscopy* **64**, 607–614 (2010).
- [18] C. Reble, I. Gersonde, C. A. Lieber, J. Helfmann, *Biomedical Optical Express* **2**, 521–532 (2011).
- [19] J. Mo, W. Zheng, Z. Huang, *Biomedical Optical Express* **1**, 17–30 (2010).
- [20] L. Wang, S. L. Jacques, and L. Zheng, *Computer Methods and Programs in Biomedicine* **47**, 131–146 (1995).
- [21] L. Wang, S. L. Jacques, and L. Zheng, *Computer Methods and Programs in Biomedicine* **54**, 141–150 (1997).
- [22] S. Wang, J. Zhao, H. Lui, Q. He, and H. Zeng, *Spectroscopy: An International Journal* **24**, 577–583 (2010).
- [23] Z. Huang, H. Zeng, I. Hamzavi, D. I. McLean, and H. Lui, *Opt. Lett.* **26**, 1782–1784 (2001).
- [24] J. Zhao, H. Lui, D. I. McLean, and H. Zeng, *Appl. Spectrosc.* **61**, 1225–1232 (2007).
- [25] E. Salomatina, B. Jiang, J. Novak, and A. N. Yaroslavsky, *J. Biom. Opt.* **11**, 064026 (2006).
- [26] I. V. Meglinski and S. J. Matcher, *Physiological Measurement* **23**, 741–753 (2002).
- [27] Bashkatov, A. N., E. A. Genina, and V. V. Tuchin, *Journal of Innovative Optical Health Sciences* **4**, 9–38 (2011).
- [28] R. R. Anderson and J. A. Parrish, *J. Invest. Dermatol.* **77**, 13–19 (1981).
- [29] J. R. Zijp, and J. J. ten Bosch, *Arch Oral Biol.* **36**, 283–289 (1991).
- [30] A. E. Profio, *Appl. Opt.* **28**, 2216–2222 (1989).
- [31] S. Wan, R. R. Anderson, and J. A. Parrish, *Photochem. Photobiol.* **34**, 493–499 (1981).
- [32] I. S. Saidi, *Transcutaneous optical measurement of hyperbilirubinemia in neonates*, PhD thesis, Rice University (US), 1992.
- [33] S. L. Jacques, M. Keijzer, in: *SPIE Proc. of Lasers in Dermatology and Tissue Welding*, Los Angeles, US, January 1991, pp. 2–13.
- [34] I. V. Meglinski and S. J. Matcher, *Computer Methods and Programs in Biomedicine* **70**, 179–186 (2003).
- [35] R. Marchesini, C. Clemente, E. Pignoli, and M. Brambilla, *J. Photochem. Photobiol. B: Biol.* **16**, 127–140 (1992).
- [36] H. Zeng, C. MacAulay, D. I. McLean, B. Palcic, and H. Lui, *Photochem. Photobiol.* **68**, 227–236 (1998).